ADVANCED FUNCTIONAL MATERIALS
www.afm-journal.de

Efficient Sb_2S_3-Sensitized Solar Cells Via Single-Step Deposition of Sb_2S_3 Using S/Sb-Ratio-Controlled $SbCl_3$-Thiourea Complex Solution

*Yong Chan Choi and Sang Il Seok**

To replace the conventional chemical bath deposition method, which is time-consuming and has a high impurity level, a chemical single-step deposition process employing a S/Sb ratio-controlled $SbCl_3$-thiourea complex solution is introduced to load Sb_2S_3 into a mesoporous TiO_2 electrode. This technique enables the fabrication of efficient and reproducible Sb_2S_3-sensitzed inorganic–organic heterojunction hybrid solar cells with hole-conducting conjugated polymers. The most efficient cell exhibits a short-circuit current density of 16.1 mA cm^{-2}, an open circuit voltage of 595.5 mV, and a fill factor of 66.5%, yielding a power conversion efficiency of ≈6.4% at standard AM1.5G condition (100 mW cm^{-2}).

1. Introduction

Antimony chalcogenides (Sb-Chs), such as Sb_2S_3,[1–4] Sb_2Se_3,[5,6] and $Sb_2(S/Se)_3$,[7] have been successfully applied as light sensitizers and absorbers in two different types of solar cells (sensitizer-architecture and planar-architecture solar cells) because of the suitability of their high absorption coefficients, band gaps in the range of 1.2–1.7 eV, air/moisture-stability, and environment-friendly features.[1–9] However, despite its potential as an efficient light sensitizer, the device efficiency remains limited to less than 10% because of impurity phases,[2d,3,5] electron/hole trap sites,[2d,10,11] and the dominant energy-loss channel caused by strong electron–phonon interactions.[12]

The method of chemical bath deposition (CBD) in aqueous solution has been widely used for the deposition of Sb_2S_3 on various substrates because it is based on the simple chemical reaction between $SbCl_3$ and $Na_2S_2O_3$ in water, and does not require sophisticated equipment or techniques.[1,2,13,14] However, some experimental factors such as the bath temperature, solution pH, and sample position within the solution must be controlled during the chemical reaction to minimize the formation of impurity phases and the concentration gradient.[3,13,14] Although all the experimental parameters are optimized, oxide/hydroxide phases, such as Sb_2O_3, SbOCl, and $Sb(OH)_3$, are inevitably formed.[3,14] These impure phases may act as one of main obstacles for the formation of pure-phase Sb_2S_3, causing sufficient electron/hole recombination centers on the surface for low device performance.[2d,3], [4] Consequently, it is a significant step for high-efficiency solar cells to develop an alternative deposition method that can produce pure-phase Sb_2S_3.[3–5]

To avoid such impurity phase formation, we previously developed the nonaqueous-phase CBD method based on the $Sb(C_2H_5NS)_2Cl_3$ single source precursor.[3] Using this method, we could successfully fabricate oxide/hydroxide-free Sb_2S_3. However, its device efficiency was less than 4%. The atomic layer deposition (ALD) method has recently gained particular attention as another alternative approach.[4] Wedemeyer et al. successfully fabricated high-purity Sb_2S_3 with uniform morphology using the ALD method, and their devices exhibited ≈2.6% in power conversion efficiency (PCE).[4a] Very recently, Kim et al. reached a high efficiency of ≈5.77% for planar-architecture solar cells using the ALD technique through precise control of the Sb_2S_3 thickness.[4b] Although Kim et al. reported better device performance as well as reproducibility in their devices compared with those fabricated using the aqueous-phase CBD method,[4b] the ALD method has several drawbacks for practical applications. One of its major limitations is its slow growth rate of 100–300 nm h^{-1}.[15] Another limitation is that the ALD process must be performed under ultrahigh vacuum condition, requiring complex and expensive instrumentation. Therefore, it is highly desirable for a potential industrial-scale process to develop a simple approach to reduce the cost and time, and produce high-quality Sb_2S_3.

Herein, we report on the fabrication of efficient Sb_2S_3-sensitized solar cells using a $SbCl_3$-thiourea (Sb-TU) complex solution. The Sb_2S_3 is easily deposited in a single-step on a mesoporous TiO_2 (mp-TiO_2)/TiO_2 blocking layer (TiO_2-BL)/F-doped SnO_2 (FTO, TEC-8). Because the loading amounts are simply controlled by tuning the mole concentration of $SbCl_3$ and thiourea (TU) in solution, our developed method does not require multiple cycles for control of the loading amounts. In addition, our method enables control of the molar ratio of S/Sb

Dr. Y. C. Choi, Prof. S. I. Seok
Center for Solar Energy Materials
Advanced Materials Division
Korea Research Institute of Chemical Technology (KRICT)
141 Gajeong-Ro, Yuseong-Gu, Daejeon
305-600, South Korea
E-mail: seoksi@krict.re.kr; seoksi@skku.edu
Prof. S. I. Seok
Department of Energy Science
Sungkyunkwan University
2066 Seobu-Ro, Jangsan-Gu, Suwon 440-746, South Korea

DOI: 10.1002/adfm.201500296

of the resultant product by adjusting the amounts of the input chemicals. Using this technique for the inorganic-organic solar cells allows us to achieve a high PCE of ≈6.4% measured under standard AM1.5G test conditions.

2. Results and Discussion

Figure 1a describes the fabrication process of the Sb_2S_3-sensitized inorganic-organic heterojunction solar cells via Sb-TU complex solution processing. First, we synthesized the Sb-TU complex solution by dissolving $SbCl_3$ and TU in N,N-dimethylformamide (DMF) at various molar ratios. Note that the solution color turned yellow, as observed in the photograph in Figure 1a-1, as $SbCl_3$ and TU were dissolved in DMF. An appearance of yellow color in the solution implies that Sb-TU complex is formed in the solution.[16] As an example, reaction (1) describes the formation process of the Sb-TU complex in the solution when the molar ratio of $SbCl_3$:TU = 1:2 is used.[16b] As the molar ratio of TU/$SbCl_3$ increased to 2, the yellow color became darker. Further increasing the Tu/$SbCl_3$ ratio did not affect the darkness of the solution color

$$SbCl_3 + 2TU \rightarrow [Sb(TU)_2]Cl_3 \quad (1)$$

To deposit the Sb_2S_3 on mp-TiO_2/TiO_2-BL/FTO, the complex solution was spin-coated (2 of Figure 1a), which allowed the solution to fill the pores of the mp-TiO_2 layer. Subsequently, the as-coated sample was thermally decomposed at 200 °C in an inert atmosphere, either Ar or N_2, until the sample color changed from transparent to orange, as shown in Figure 1a-3. The thermally decomposed sample exhibited an absorption edge of ≈575 nm (≈2.15 eV), as represented by the black line in Figure 1b, and no crystalline peaks except mp-TiO_2 and FTO peaks appeared in the X-ray diffraction (XRD) pattern (black line of Figure 1c). The XRD pattern of the sample deposited on glass further confirmed the absence of any crystalline peaks, as shown in Figure S1, Supporting Information. The three different characteristics, namely, the orange color,[17a] absorption edge near 575 nm,[17b] and very broad XRD pattern, indicate that the amorphous phase was formed after the thermal decomposition (TD) step. Note that for control of the Sb_2S_3-loading amount, repeating two cycles of spin coating and TD was not required, unlike the case of our previous work on

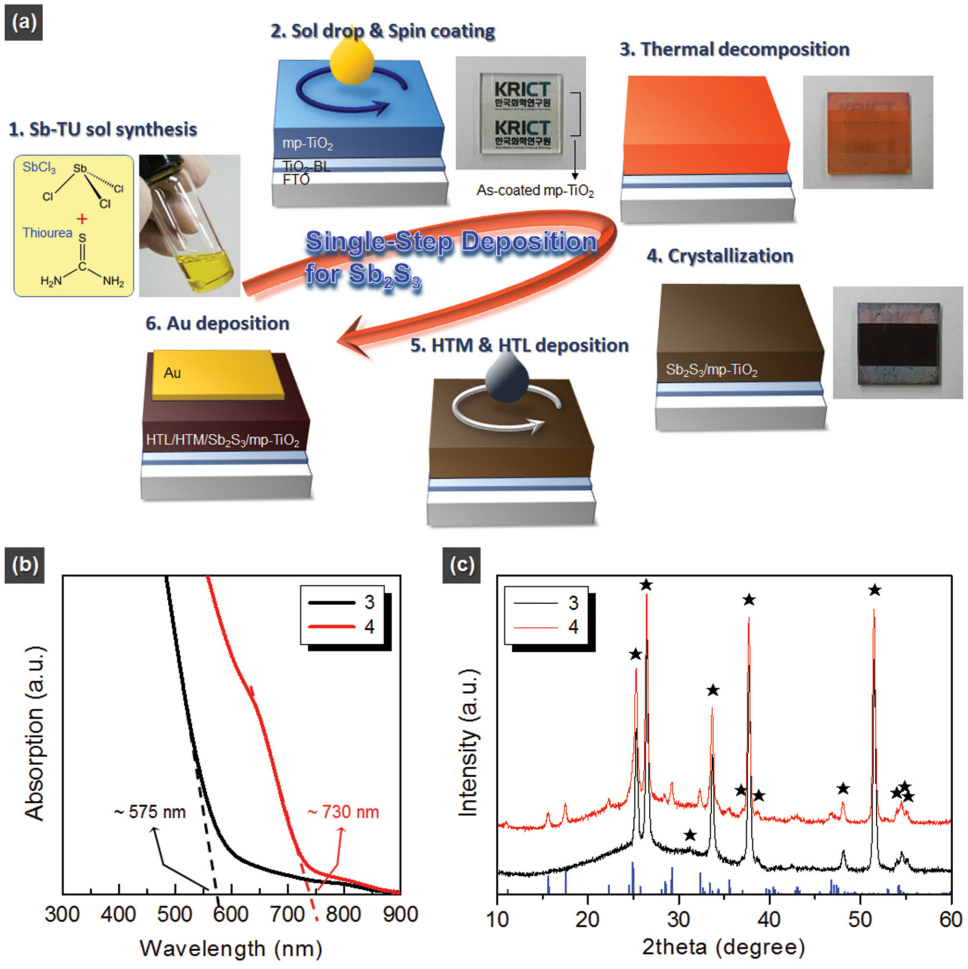

Figure 1. a) Schematic diagram of the fabrication process of our devices via Sb-TU complex solution processing. The photographs after steps of 1–4 are shown on the right side of each figure. b) UV–vis absorption spectra and c) XRD patterns of the samples obtained after steps 3 and 4. The peaks induced from mp-TiO_2 and FTO are denoted by black stars in (c). The standard stibnite Sb_2S_3 structure file (JCPDS No. 42-1393) is plotted as the blue column in (c).

Sb_2Se_3-sensitized cells where the cells were fabricated using the Sb_2Se_3-SSP method.[5] The amount was simply controlled by adjusting the mole concentration of the input chemicals (see Figures S2, S3, and Table S1, Supporting Information). After the TD step, the sample was annealed at 300 °C for 10 min in an Ar atmosphere (Figure 1a-4). The sample color turned to dark brown after the annealing step. The annealed sample had an orthorhombic Sb_2S_3 structure with a band gap of ≈1.7 eV (absorption edge of ≈730 nm), as represented by the red lines of Figure 1b,c. Afterwards, the hole-transporting material and layer (HTM and HTL) were sequentially deposited on (mp-TiO_2 layer infiltrated with Sb_2S_3)/TiO_2-BL/FTO (Figure 1a-5). In this study, the thiophene-based conjugated polymers, either poly(2,6-(4,4-bis-(2-ethylhexyl)-4*H*-ctckioebta[2,1-*b*;3,4-*b*']dithiophene)-alt-4,7(2,1,3-benzothiadiazole)) (PCPDTBT) or poly(3-hexylthiophene) (P3HT), were used as HTMs for their intimate interactions with Sb_2S_3.[2b] The poly(3.4-ethylenedioxythiophene)-poly(styrenesulfonate) (PEDOT:PSS) was used as a HTL. Finally, Au electrode was deposited by thermal evaporation (Figure 1a-6).

To verify the distribution of Sb_2S_3 along the depth of the mp-TiO_2 layer, we investigated the morphology and elemental composition along the cross-section of devices using a field emission scanning electron microscope (FESEM) equipped with an energy-dispersive X-ray (EDX) spectrometer. The Sb_2S_3 was deposited on the mp-TiO_2 layer using the Sb-TU complex solution composed of 1 mmol $SbCl_3$ in 1 mL of DMF ($SbCl_3$:TU = 1:2). The cross-sectional FESEM image (**Figure 2**a) reveals that the device consisted of three distinct layers, namely, (L1) a mp-TiO_2 layer infiltrated with Sb_2S_3/HTM(L), (L2) a TiO_2-BL, and (L3) a FTO layer. The similar morphology of L1 compared with that of the bare mp-TiO_2 layer (inset image of Figure 2a) suggests that the pores of the mp-TiO_2 layer were uniformly filled with Sb_2S_3 and HTM/HTL by our method (see also Figure S4, Supporting Information). The EDX line scan profile shows the uniform distribution of Sb and S elements along the L1 layer, as observed in Figure 2b, confirming the uniform deposition of Sb_2S_3 inside the pores of the mp-TiO_2 layer.

In addition to the uniform distribution of Sb_2S_3, we also evaluated the structural variation of as-formed Sb_2S_3 along the depth with the grazing incidence XRD (GIXRD) technique. We chose the sample composed of (mp-TiO_2 layer infiltrated with Sb_2S_3)/TiO_2-BL/FTO for the GIXRD measurement to avoid misinterpretation with the XRD peaks of HTM/HTL. Because the GIXRD measurement is performed at a fixed incidence-angle (α) while only the detector is moved over a 2θ range of interest (Figure 2c), the penetration depth of X-rays into the sample can be controlled by selecting an appropriate value of

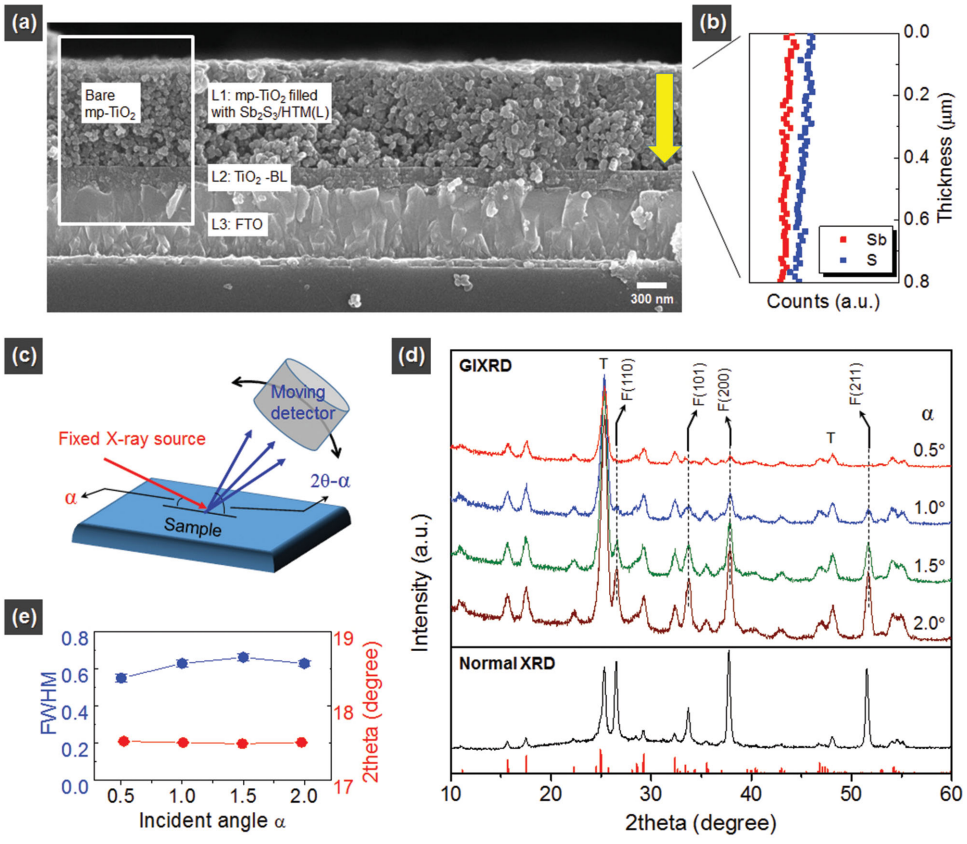

Figure 2. a) Cross-sectional FESEM image of a typical device and b) EDX line scan profile along the L1 layer. For the EDX line scan profile analysis, the sample was deposited on glass (not FTO) to avoid misinterpretation between two elements, i.e., Sb of Sb_2S_3 and Sn of FTO. c) A scheme for GIXRD measurement. d) GIXRD patterns as a function of incident angle α and normal XRD pattern of the sample "(mp-TiO_2 infiltrated with Sb_2S_3)/TiO_2-BL/FTO." The standard stibnite Sb_2S_3 structure file (JCPDS No. 42-1393) is plotted as a red column in (d). T indicates the mp-TiO_2 phase in (d). e) Graph for 2θ and FWHM values obtained from Sb_2S_3 (120) plane as a function of α.

α.[18] Thus, this technique enables structural variations along the sample depth to be detected by controlling α.[18] Figure 2d presents the GIXRD patterns as a function of α with normal XRD pattern. At a low α of 0.5°, only two phases of Sb_2S_3 and mp-TiO_2 without the underlying FTO phase were detected, unlike the normal XRD pattern. This result implies that the structural information was obtained near the sample surface at the low angle. The GIXRD patterns collected at different α show that the FTO peaks, as denoted by F(###) in Figure 2d, started to appear and their intensities gradually increased as α increased. These results indicate that the patterns derived from the surface to bottom of the sample were obtained with increasing α. To compare the structural properties along the depth, we investigated changes of 2θ and full width at half maximum (FWHM) values obtained from the XRD peaks of Sb_2S_3 as a function of α. As an example, the data on the Sb_2S_3 (120) peak was plotted in the graph of Figure 2e. The graph shows that two values of 2θ and FWHM are very similar as 17.51 ± 0.01° and 0.61 ± 0.04°, respectively, regardless of α. From the result, we see that the structure of Sb_2S_3 along the depth of the mp-TiO_2 layer is identical.

It was reported that Sb_2S_3 can be a sulfur-deficient as a consequence of sulfur loss and oxidized during the crystallization process at high temperature.[2d] In this regard, current method enables an exact ratio of S/Sb in the final product by controlling the input ratio of $SbCl_3$:TU. The normalized S amount of the resultant products against CBD derived Sb_2S_3 (red line) is plotted as a function of the $SbCl_3$:TU = 1:x ratio in the graph of **Figure 3**a. We normalized all data by setting S amount of the stoichiometric Sb_2S_3 as 100. In the CBD process, it is not easy to control the S/Sb ratio of the Sb_2S_3 phase formed from chemical reaction between $SbCl_3$ and $Na_2S_2O_3$ in water.[14] In contrast, the S/Sb ratio of final product could be readily controlled by adjusting the input ratio in the current method. As observed in Figure 3a, the S amount of final product gradually increased with increasing ratio of $SbCl_3$:TU. However, the use of excess TU exceeding 1.8 in the ratio of $SbCl_3$:TU resulted in the formation of free sulfur because of S-rich condition, as will be shown later. Figure 3b shows the variation of short-circuit current density (J_{SC}), open-circuit voltage (V_{OC}), fill factor (FF), and resulting PCE with the input TU/$SbCl_3$ ratio. All device performances are summarized in **Table 1**. For each device, the complex solutions were synthesized as follows: the 1.0 mmol $SbCl_3$ was dissolved in 1 mL of DMF, and then, TU was added at various molar ratios to the $SbCl_3$ solution for the synthesis of the Sb-TU complex solution. In other words, the amount of Sb source was fixed in 1.0 mmol where the cell performance is relatively highest (See Figure S3, Supporting Information). Upon increasing the TU amount, J_{SC} value slightly increased and then saturated. Unlike the change of J_{SC}, the two factors of V_{OC} and FF reached maximum values at the specific ratio of $SbCl_3$:TU = 1:1.8. Therefore, the highest PCE was obtained at the ratio of 1:1.8.

Table 1. Effects of $SbCl_3$:TU ratio on photovoltaic performance.

$SbCl_3$:TU ratio	J_{SC} [mA cm^{-2}]	V_{OC} [mV]	FF [%]	PCE [%]	R_{SH}/R_S [Ω cm^2]
1:1.4	12.2	475.4	61.7	3.8	582.4/7.1
1:1.6	12.0	487.4	66.4	4.1	1135.4/6.5
1:1.8	12.7	493.4	66.5	4.4	1217.3/6.8
1:2.0	13.1	493.4	61.6	4.2	644.7/7.8
1:2.2	13.0	487.4	59.4	3.9	541.8/8.9

To gain further insight into photovoltaic performance with the molar ratio of $SbCl_3$:TU, we investigated the effects of the ratio on the absorption properties and surface states of the samples of "(mp-TiO_2 layer filled with Sb_2S_3)/TiO_2-BL/FTO" using UV–vis absorption spectroscopy and X-ray photoelectron spectroscopy (XPS), respectively. As observed in **Figure 4**a, the absorption gradually increased upon increasing the ratio of TU/$SbCl_3$. This result indicates that the amount of Sb_2S_3 upon increasing the TU amount is increased. Thus, it can be deduced that increasing ratio of TU/$SbCl_3$ results in increased J_{SC}, because of the increased formation of Sb_2S_3 at the sulfur-sufficient condition. These results also suggest that the Sb_2S_3 loading amounts can be slightly tuned by the input molar ratio. Figure 4b shows the high-resolution core-level XPS spectra of Sb $3d_{3/2}$. Note that the Sb 3d in XPS generally consists of two main peaks of Sb $3d_{3/2}$ and Sb $3d_{5/2}$ due to the spin-orbit coupling; however, the latter peak was not considered in the peak analysis to avoid misinterpretation because of highly overlapped binding energy between the Sb $3d_{5/2}$ peak (529.7–530.3 eV)[2d,19] of Sb_2S_3 and the O 1s peak (≈530.0 eV)[20] of mp-TiO_2. As can be observed from Figure 4b, the single peak, corresponding to the Sb_2S_3 phase (red dotted line and arrow), [2d,19] without oxide phase (black dotted line and arrow) was detected for all samples. This result indicates that the oxide phase was not formed on the surface of Sb_2S_3, suggesting that a high-purity Sb_2S_3 phase can be produced using the current method.

At high TU amount conditions (denoted as S-excess region in Figure 3a), the new peak located at the binding energy of

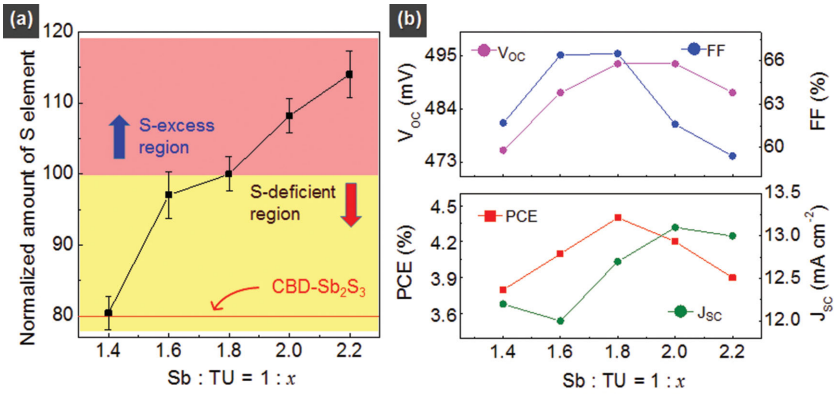

Figure 3. a) Normalized amount of S element in resultant Sb_2S_3 and b) a graph of the values of V_{OC}, FF, J_{SC}, and PCE as a function of the $SbCl_3$:TU ratio. The ratios were obtained using EDX. The data of CBD-Sb_2S_3 was obtained from the sample of Sb_2S_3 fabricated using the aqueous CBD method. The S-excess and S-deficient regions are marked with pink- and yellow-filled areas in (a), respectively.

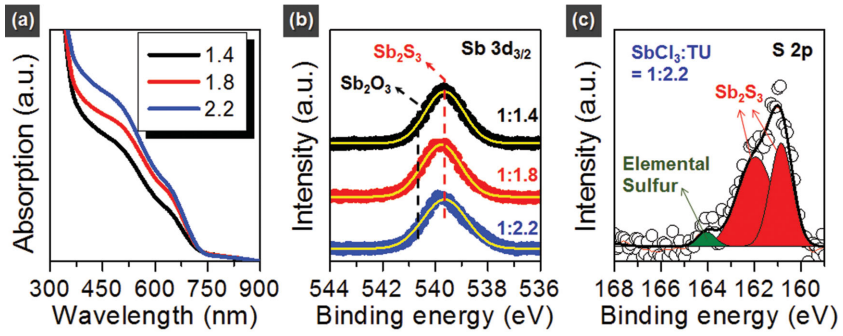

Figure 4. Effects of $SbCl_3$:TU ratio on a) UV–vis absorption spectra, and b,c) XPS spectra. High resolution core-level XPS spectra of b) Sb $3d_{3/2}$ and c) S 2p. The fitted curves are shown as yellow lines in (b).

163.9 eV, corresponding to the elemental sulfur,[21] was appeared (expressed by the green-filled peak in Figure 4c), and its intensity was increased with further increase of TU. Because the elemental sulfur is a polyatomic nonmetal, it may act as a barrier to charge flow in the solar devices. Thus, this increase of sulfur caused an increase of series resistance (R_S) with increasing TU amount, as shown in Table 1. In addition, the elemental sulfur may cause unexpected defects, leading to decreased shunt resistance (R_{SH}). Consequently, the presence of elemental sulfur may results in degradation of the two factors of FF and V_{OC} owing to increased R_S and decreased R_{SH}, respectively,[22] which also led to a decrease of PCE under sulfur-excess conditions despite the higher J_{SC}, as observed in Figure 3b and Table 1. Although the other experimental factors, such as the correlated changes of the solution viscosity and pore-filling behaviors, may contribute to the device performance, it is obvious that the S/Sb ratio is one of the key factors affecting the device efficiency in the current system. The S/Sb ratio effect described here is the first demonstration of all Sb-chalcogenides-based solar cells to the best our knowledge.

In addition to the S/Sb ratio, we observed that the HTM concentration was another critical factor for device performance. **Figure 5** and **Table 2** show the effects of the HTM concentration on the device performance. In these devices, the complex solution of 1.0 mmol $SbCl_3$ with the ratio $SbCl_3$:TU = 1:1.8 in 1 mL of DMF was used. The PCPDTBT was used as a HTM, and its concentration in 1 mL of 1,2-dichlorobenzene was varied. As the HTM concentration increased to 25 mg mL^{-1}, the V_{OC} increased (Figure 5a and Table 2), suggesting that

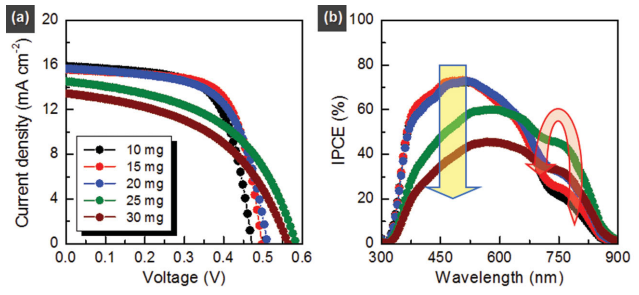

Figure 5. Effects of PCPDTBT HTM concentration in 1 mL of 1,2-dichlorobenzene on the photovoltaic performance: a) *J–V* curves and b) IPCE spectra.

the thicker HTM may act as effective barrier for back-flow of photogenerated electrons. By contrast, the two factors of J_{SC} and FF were reduced at higher concentration of >20 mg mL^{-1}, leading to decreased PCE. In the incident-photon-to-current-efficiency (IPCE) spectrum of Figure 5b, the IPCE also increased with increasing HTM concentration to 20 mg mL^{-1}. However, in the shorter wavelength region below 600 nm, the IPCE was also observed to decrease at high concentration of >20 mg mL^{-1}. These results observed at such high HTM concentration may be attributed to the incomplete filling of HTM inside pores of the layer of "mp-TiO_2 filled with Sb_2S_3." Therefore, the efficient PCE could be obtained at the specific HTM concentration region of 15–20 mg mL^{-1}. Similar variation depending on the concentration was also observed for the P3HT HTM, as shown in Figure S5 and Table S2, Supporting Information. Although further investigations are required to clearly interpret the correlation between the HTM concentration and photovoltaic performance, the results obviously reveal that the optimum HTM concentration for high performance is present. It should be noted that the devices fabricated in the absence of Sb_2S_3 showed very low efficiency regardless HTM species (see Figure S6, Supporting Information), implying that the contribution of HTM as a light absorber is ignorable without Sb_2S_3.

To further enhance the device performance of our cells, we repeated the fabrication procedure after fine-tuning some experimental parameters, such as the mp-TiO_2 thickness, mole concentration, spin coating conditions, HTM species, and addition of $PC_{60}BM$ ([6,6]-phenyl-C_{60}-butyric acid methyl ester) into the HTM solution. The best sample was fabricated under the conditions of 1 μm thick mp-TiO_2, 1.0–1.1 M solution concentration with $SbCl_3$:TU ratio of 1:1.8, and PCPDTBT:$PC_{60}BM$ (20:5 mg mL^{-1}) HTM. Here, the $PC_{60}BM$ was used as an electron channel bridging mp-TiO_2 and PCPDTBT for efficient electron injection into TiO_2 or Sb_2S_3.[2c] The photocurrent density–voltage (*J–V*) curve and IPCE spectrum of the best performing device are presented in **Figure 6** and **Table 3**. The champion cell exhibited a J_{SC} of 16.1 mA cm^{-2}, V_{OC} of 595.5 mV, and FF of 66.5%, corresponding to a PCE of 6.4% under standard AM 1.5G conditions (100 mW cm^{-2}). The average PCE value was 5.3 ± 0.4% in PCE, demonstrating its potential as an efficient approach. In addition, no hysteresis depending on the scanning direction and delay-time in the *J–V* curves was observed, as shown in Figure S7, Supporting Information. For the IPCE

Table 2. Summary of photovoltaic performance obtained from Figure 5a.

Concentration [mg mL^{-1}]	J_{SC} [mA cm^{-2}]	V_{OC} [mV]	FF [%]	PCE [%]
10	15.9	472.9	61.6	4.9
15	15.6	497.0	64.3	5.3
20	15.7	509.1	59.4	5.0
25	14.5	581.4	47.5	4.2
30	13.4	563.3	45.0	3.6

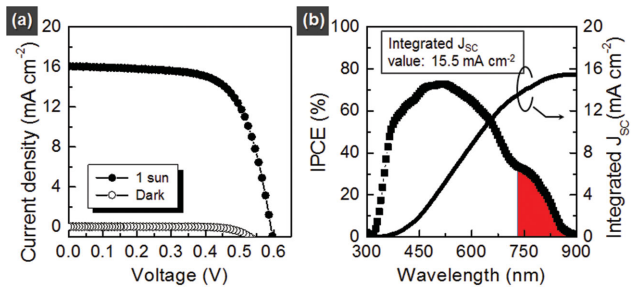

Figure 6. a) *J–V* curve and b) IPCE spectrum of the champion device. The contribution by HTM was expressed by red-filled area in (b).

spectrum, the photocurrent contribution was extended to 900 nm, and the J_{SC} value integrated from the IPCE agreed well with that measured by the *J–V* curve. For P3HT HTM, the plateau shape of over 70% between 370 and 650 nm was obtained in the IPCE spectrum, as observed in Figure S8, Supporting Information. Although additional light-harvesting of low band-gap HTMs through the formation of electron channels in a hole-conducting material was previously reported,[2c] the contribution of PCPDTBT to IPCE is noticeable, as denoted by the red-filled area in Figure 6b. This result suggests that the near-IR light, which cannot be absorbed by Sb_2S_3 only, can be efficiently utilized by simply applying a proper low-band gap HTM to the current system without replacement of Sb_2S_3 to low-bandgap Sb-Chs, such as Sb_2Se_3.[5] Therefore, it is expected that higher J_{SC} can be achieved while maintaining V_{OC} in the current system if a suitable low band-gap HTM is applied, also providing one possible solution to solve the low V_{OC} of <0.4 V problem faced in Sb_2Se_3-sensitized devices.[5] Efforts are in progress to find an optimum low-bandgap HTM.

The Sb-TU complex solution processing presented here provides a means to achieve excellent photovoltaic performance. The PCE of 6.4% observed in the best device is comparable to our previous record value (6.3%) achieved in non-surface-treated Sb_2S_3 devices.[2c] These facts suggest that the current method is a competitive approach toward the development of high-efficiency Sb_2S_3 solar cells. In addition, our method opens a new route for the fabrication of various metal chalcogenides (M-Chs)-based photovoltaic devices; because some desired M-Chs may be readily fabricated using the M-TU complex solution processing described here. Practically, we could very recently successfully fabricate different types of M-Chs-based solar cells, such as $CuSbS_2$.[23]

3. Summary

We demonstrated a simple method based on Sb-TU complex solution processing for the application to Sb_2S_3-sensitized inorganic-organic heterojunction solar cells. Using this method, we could successfully deposit Sb_2S_3 on mp-TiO_2/TiO_2-BL/FTO in a single step. We observed that the input ratio of the chemicals and HTM concentration were key factors affecting device performance. The most efficient device was obtained under specific conditions of the ratio of $SbCl_3$:TU = 1:1.8 and PCPDTBT HTM concentration of 15–20 mg mL^{-1}. The best device exhibited a high device efficiency of 6.4%, measured under AM 1.5G standard conditions. Therefore, we believe that current method can be easily extended to solar cells based on various metal chalcogenides including binary, ternary, and quaternary materials.

Table 3. Photovoltaic performances of the champion device obtained from Figure 6a and average data.

	J_{SC} [mA cm^{-2}]	V_{OC} [mV]	FF [%]	PCE [%]
Champion	16.1	595.5	66.5	6.4
Average[a)]	16.1 ± 0.9	543.7 ± 15.0	60.7 ± 2.2	5.3 ± 0.4

[a)]Average data were obtained from 50 independently fabricated cells.

4. Experimental Section

Synthesis of Sb-TU Complex Solution: A homogeneous Sb_2S_3 precursor solution was prepared via a simple Sb-TU complex synthesis in organic solvent. Antimony chloride $SbCl_3$ (≥99.0 %, Sigma-Aldrich) and TU (NH_2CSNH_2, ≥99.0 %, Sigma-Aldrich) were selected as the starting chemicals. DMF was used as an organic solvent. First, the $SbCl_3$ (various moles of 0.5–1.4 mmol) was dissolved in 1 mL of DMF and stirred for at least 30 min. Then, TU was added to the $SbCl_3$ solution in a molar ratio of $SbCl_3$:TU = 1:1.0–2.4 and stirred for 30 min to synthesize the Sb-TU complex solution. After complete dissolution of TU, the solution color was yellow, where its darkness was dependent on the TU amount. The final solution was very stable for several months at ambient conditions.

Preparation of mp-TiO_2/TiO_2-BL/FTO: A thin compact TiO_2-BL of ≈200 nm thickness was first deposited on a precleaned FTO using five repeated cycles of spin coating with 0.1 M TiO_2 sol–gel solution and subsequent drying at 200 °C. The TiO_2 precursor solution was synthesized by reacting titanium isopropoxide, nitric acid, deionized water, and ethanol. Then, the mp-TiO_2 with thickness ranges of 800–1800 nm was deposited by the screen-printing method with custom-made TiO_2 paste. A TiO_2 paste was prepared by mixing 6 g of the TiO_2 nanoparticles (average diameter 50 nm, anatase), in 100 mL of ethanol, 30 g of a 10 wt% ethanolic solution of ethyl cellulose, and 30 g of terpineol, and then homogenizing by ultrasonic irradiation.[2,3,5] Subsequently, as-deposited mp-TiO_2/TiO_2-BL/FTO substrates were annealed at 550 °C for 2 h in air for crystallization of TiO_2-BL, intimate contact at each interface, and removal of organic residues from mp-TiO_2. The samples were finally post-treated with 40×10^{-3} M $TiCl_4$-assisted solution processing.[2d]

Fabrication of Solar Cells, Characterization, and Measurement of Photovoltaic Performance: The fabrication procedure of solar cells is described in the text with Figure 1. The morphology, structure, absorption property, and surface state were characterized by FESEM, XRD, UV–vis absorption spectroscopy, and XPS, respectively. All the XPS binding energies were calibrated with the C–C peak at 284.6 eV in the C 1*s* spectra. The *J–V* curves were measured with a metal mask that was 0.1225 cm^2 in area using a solar simulator (Newport, Oriel Class A, 91195A) with a source meter (Keithley 2400) at 100 mA cm^{-2} illumination AM 1.5 G and a calibrated Si-reference cell certificated by NREL. The IPCE spectra were measured using a power source (Newport 300 W Xenon lamp, 66920) with a monochromator (Newport Cornerstone 260) and a multimeter (Keithley 2001).

Supporting Information

Supporting Information is available from the Wiley Online Library or from the author.

Acknowledgements

This work was supported by the Global Research Laboratory (GRL) Program, the Global Frontier R&D Program on Center for Multiscale

Energy System funded by the National Research Foundation in Korea, and by a grant from the KRICT 2020 Program for Future Technology of the Korea Research Institute of Chemical Technology (KRICT), Republic of Korea. Y.C.C. thanks Eun Joo Yeom for her assistance of experiments.

Received: January 23, 2015
Revised: March 8, 2015
Published online: April 7, 2015

[1] a) Y. Itzhaik, O. Niitsoo, M. Page, G. Hodes, *J. Phys. Chem. C* **2009**, *113*, 4254; b) S.-J. Moon, Y. Itzhaik, J.-H. Yum, S. M. Zakeeruddin, G. Hodes, M. Grätzel, *J. Phys. Chem. Lett.* **2010**, *1*, 1524; c) S. Ito, K. Tsujimoto, D.-C. Nguyen, K. Manabe, H. Nishino, *Int. J. Hydrogen Energy* **2013**, *38*, 16749.

[2] a) J. A. Chang, J. H. Rhee, S. H. Im, Y. H. Lee, H.-j. Kim, S. I. Seok, M. K. Nazeeruddin, M. Gratzel, *Nano Lett.* **2010**, *10*, 2609; b) S. H. Im, C.-S. Lim, J. A. Chang, Y. H. Lee, N. Maiti, H.-J. Kim, M. K. Nazeeruddin, M. Grätzel, S. I. Seok, *Nano Lett.* **2011**, *11*, 4789; c) J. A. Chang, S. H. Im, Y. H. Lee, H.-j. Kim, C.-S. Lim, J. H. Heo, S. I. Seok, *Nano Lett.* **2012**, *12*, 1863; d) Y. C. Choi, D. U. Lee, J. H. Noh, E. K. Kim, S. I. Seok, *Adv. Funct. Mater.* **2014**, *24*, 3587.

[3] N. Maiti, S. H. Im, C.-S. Lim, S. I. Seok, *Dalton Trans.* **2012**, *41*, 11569.

[4] a) H. Wedemeyer, J. Michels, R. Chmielowski, S. Bourdais, T. Muto, M. Sugiura, G. Dennler, J. Bachmann, *Energy Environ. Sci.* **2013**, *6*, 67; b) D.-H. Kim, S.-J. Lee, M. S. Park, J.-K. Kang, J. H. Heo, S. H. Im, S.-J. Sung, *Nanoscale* **2014**, *6*, 14549.

[5] Y. C. Choi, T. N. Mandal, W. S. Yang, Y. H. Lee, S. H. Im, J. H. Noh, S. I. Seok, *Angew. Chem. Int. Ed.* **2014**, *53*, 1329.

[6] a) T. T. Ngo, S. Chavhan, I. Kosta, O. Miguel, H.-J. Grande, R. N. Tena-Zaera, *ACS Appl. Mater. Interfaces* **2014**, *6*, 2836; b) Y. Zhou, M. Leng, Z. Xia, J. Zhong, H. Song, X. Liu, B. Yang, J. Zhang, J. Chen, K. Zhou, *Adv. Energy Mater.* **2014**, *4*, 1301846; c) M. Leng, M. Luo, C. Chen, S. Qin, J. Chen, J. Zhong, J. Tang, *Appl. Phys. Lett.* **2014**, *105*, 083905.

[7] Y. C. Choi, Y. H. Lee, S. H. Im, J. H. Noh, T. N. Mandal, W. S. Yang, S. I. Seok, *Adv. Energy Mater.* **2014**, *4*, 1301680.

[8] M. R. Filip, C. E. Patrick, F. Giustino, *Phys. Rev. B* **2013**, *87*, 205125.

[9] M. Y. Versavel, J. A. Haber, *Thin Solid Films* **2007**, *515*, 7171.

[10] a) P. P. Boix, Y. H. Lee, F. Fabregat-Santiago, S. H. Im, I. Mora-Sero, J. Bisquert, S. I. Seok, *ACS nano* **2011**, *6*, 873; b) D. U. Lee, S. W. Pak, S. G. Cho, E. K. Kim, S. I. Seok, *Appl. Phys. Lett.* **2013**, *103*, 023901.

[11] a) J. A. Christians, P. V. Kamat, *ACS Nano* **2013**, *7*, 7967; b) J. A. Christians, D. T. Leighton, P. V. Kamat, *Energy Environ. Sci.* **2014**, *7*, 1148.

[12] W. K. Chong, G. Xing, Y. Liu, E. L. Gui, Q. Zhang, Q. Xiong, N. Mathews, C. K. Gan, T. C. Sum, *Phys. Rev. B* **2014**, *90*, 035208.

[13] a) M. Nair, Y. Pena, J. Campos, V. Garcia, P. Nair, *J. Electrochem. Soc.* **1998**, *145*, 2113; b) S. Messina, M. Nair, P. Nair, *Thin Solid Films* **2007**, *515*, 5777.

[14] S. Pawar, B. Pawar, J. Kim, O.-S. Joo, C. Lokhande, *Curr. Appl. Phys.* **2011**, *11*, 117.

[15] M. Leskelä, M. Ritala, *Angew. Chem. Int. Ed.* **2003**, *42*, 5548.

[16] a) J. Yang, J.-h. Zeng, S.-H. Yu, L. Yang, Y.-H. Zhang, Y.-T. Qian, *Chem. Mater.* **2000**, *12*, 2924; b) I. Ozturk, N. Kourkoumelis, S. Hadjikakou, M. Manos, A. Tasiopoulos, I. Butler, J. Balzarini, N. Hadjiliadis, *J. Coord. Chem.* **2011**, *64*, 3859.

[17] a) K. A. Mady, S. Hammad, W. Soliman, *J. Mater. Sci.* **1987**, *22*, 4153; b) F. Aousgi, M. Kanzari, *J. Optoelectron. Adv. Mater.* **2010**, *12*, 227.

[18] S. Schorr, C. Stephan, T. Tomdahl, Roland Mainz, in *Advanced Characterization Techniques for Thin Film Solar Cells* (Eds.: D. Abou-Ras, T. Kirchartz, U. Rau), Wiley-VCH, Weinheim **2011**, p. 354.

[19] a) V. Zakaznova-Herzog, S. Harmer, H. Nesbitt, G. Bancroft, R. Flemming, A. Pratt, *Surf. Sci.* **2006**, *600*, 348; b) Q. Han, S. Sun, D. Sun, J. Zhu, X. Wang, *RSC Adv.* **2011**, *1*, 1364; c) K. Xiao, Q.-Z. Xu, K.-H. Ye, Z.-Q. Liu, L.-M. Fu, N. Li, Y.-B. Chen, Y.-Z. Su, *ECS Solid State Lett.* **2013**, *2*, P51.

[20] G. Silversmit, H. Poelman, D. Depla, N. Barrett, G. B. Marin, R. De Gryse, *Surf. Interface Anal.* **2006**, *38*, 1257.

[21] A. Rossi, D. Atzei, S. Da Pelo, F. Frau, P. Lattanzi, K. England, D. Vaughan, *Surf. Interface Anal.* **2001**, *31*, 465.

[22] M. A. Green, *Solar Cells: Operating Principles, Technology, and System Applications*, Prentice-Hall, Kensington **1982**.

[23] Y. C. Choi, E. J. Yeom, T. K. Ahn, S. I. Seok, *Angew. Chem. Int. Ed.* **2015**, *54*, 4005.